An idealized $1\frac{1}{2}$-layer isentropic model with convection and precipitation for satellite data assimilation research. Part I: model dynamics

Luca Cantarello*[1], Onno Bokhove†[1], and Steven Tobias[1]

[1]School of mathematics, University of Leeds, Leeds, UK

Abstract

An isentropic $1\frac{1}{2}$-layer model based on modified shallow water equations is presented, including terms mimicking convection and precipitation. This model is an updated version of the isopycnal single-layer modified shallow water model presented in Kent et al. (2017). The clearer link between fluid temperature and model variables together with a double-layer structure make this revised, isentropic model a more suitable tool to achieve our future goal: to conduct idealized experiments for investigating satellite data assimilation. The numerical model implementation is verified against an analytical solution for stationary waves in a rotating fluid, based on Shrira's methodology for the isopycnal case. Recovery of the equivalent isopycnal model is also verified for $\kappa = R/c_p = 1$, both analytically and numerically. With convection and precipitation added, we show how complex model dynamics can be achieved exploiting rotation and relaxation to a meridional jet in a periodic domain. This solution represents a useful reference simulation or "truth" in conducting future (satellite) data-assimilation experiments, with additional atmospheric conditions and data. A formal analytical derivation of the isentropic $1\frac{1}{2}$-layer model from a 2-layer isetropic model without convection and precipitation is shown in a companion paper (Part II).

1 Introduction

Satellites are one of the main sources of observations in atmospheric data assimilation (DA). Since they became part of the Global Observing System (GOS) in 1979, they have greatly improved the quality of weather forecasting, especially in the Southern Hemisphere (Simmons and Hollingsworth, 2002; Rabier, 2005).

The preeminent position of satellite observations in most weather forecasting systems continues the need for research on how to expand their use in a more efficient and impactful way. Recently, for example, more resources have been directed towards the assimilation of all-sky observations (Geer et al., 2017, 2018; Migliorini and Candy, 2019). However, because of the high computational resources required to run an operational DA scheme and the huge amount of satellite data available today, research in satellite data assimilation using operational schemes can be a challenging task. In this regard, the development and the use of a wide range of simpler models has been explored in recent years to support DA research (not limited to satellite research). These efforts comprised both idealised low-order models of the atmosphere and models of intermediate complexity (Ehrendorfer and Errico, 2008; Vetra-Carvalho et al., 2011; Rudd et al., 2012; Stewart et al., 2013; Würsch and Craig, 2014; Smith et al., 2015; Petrie et al., 2017; Zaplotnik et al., 2018; Bannister, 2020).

Our previous research has led to the development of an idealized model for convection and precipitation, henceforth called *modRSW*, based on augmented shallow-water equations (Kent et al., 2017; Kent, 2016), which extended the model developed by Würsch and Craig (2014). In later work, that model was used to conduct idealized forecast-assimilation experiments proving its suitability and relevance for Numerical Weather Prediction (NWP) data assimilation research (Kent et al., 2020). Further work concerns the inclusion of idealized satellite data-assimilation simulations. Unfortunately, limitations for *modRSW*'s use in satellite DA have emerged and an extension of the model is necessary. Hence, in this paper, modifications to the model are undertaken in order to make it suitable for satellite DA research.

One of the most impactful types of satellite data used in operational NWP systems are passive observations of emitted thermal radiation coming from the Earth's surface and atmosphere. This radiation can be related to the temperature of the emitting source (and vice versa) by exploiting the principles of radiative transfer and black body radiation. Therefore, in order to perform sensible satellite data assimilation in an idealized fashion, it is essential that either (i) the background model includes temperature among the prognostic variables or (ii) one (or more) of the model variables can be readily related to temperature.

*Corresponding author: mmlca@leeds.ac.uk

†Corresponding author: o.bokhove@leeds.ac.uk

Regarding the latter issue, the *modRSW* model is not particularly well-suited, since it does not include temperature among its prognostic variables, and even though a simple diagnostic relationship between fluid depth and temperature can be formulated (based on the hydrostatic equilibrium and the ideal gas law), this leads to some scaling issues in which DA-relevant model dynamics can be achieved only for unrealistic values of the temperature. A second big limitation posed by the *modRSW* model is the fact that it is based on a single layer of fluid, which hampers the possibility of working with vertically-complex observations, an essential feature that needs to be replicated in the context of satellite DA.
Given the above issues, we have formulated the following modifications of the modRSW model:

i. we use a 1.5-layer model instead of a single layer model, adding a passive layer on top, nearly at rest, and effectively capped by a rigid lid; and,

ii. we replaced the isopycnal model, with its uniform layer density, by an isentropic model, in which the potential temperature (or the entropy) is constant within each layer.

Although the first modification would require only the replacement of the acceleration due to gravity with a so-called reduced gravity g', the second requires the derivation of a somewhat different set of equations. However, due to both its length and complexity, we will cover the formal mathematical derivation of such model, together with a discussion of the physical scaling, in a separate companion paper (Part II).
The newly derived model, denoted by *ismodRSW*, incorporates a much more robust definition of temperature for each layer, since the temperature T for an isentropic fluid is linked to the definition of its potential temperature θ:

$$\theta = T\left(\frac{p_r}{p}\right)^{\kappa} \Longrightarrow T = \theta\left(\frac{p}{p_r}\right)^{\kappa} = \theta\eta^{\kappa}, \tag{1}$$

in which p is the pressure, p_r a reference pressure and $\kappa = R/C_p$ the ratio between the specific gas constant for dry air ($R = 287\,\mathrm{JKg^{-1}K^{-1}}$) and its specific heat capacity at constant pressure ($c_p = 1004\,\mathrm{JKg^{-1}K^{-1}}$), with $\eta = p/p_r$ a key variable in the isentropic model's lower layer. $\Pi = \eta^{\kappa}$ is also referred in the literature as the *Exner function*. Using an isentropic model also becomes crucial in solving the scaling issues arising in the isopycnal model, as hinted at in a paper from Pan and Smith (1999), where the reduced gravity for an isentropic configuration is used instead to estimate g' from observations in their classic (isopycnal) reduced-gravity shallow-water model. Additionally, the presence of the second, upper layer will help to increase the vertical complexity with which we describe the atmosphere yielding a more realistic test-bed for satellite data assimilation.
We note here that there are no further changes to the model setup apart from the two modifications mentioned above: the essential functioning and dynamics of the model remain similar to those of the *modRSW*, including the threshold mechanism used to simulate convection and precipitation. However, the presence of bottom topography will not be considered in this paper.
The structure of the paper is as follows. In section 2, the $1\frac{1}{2}$-layer model without convection and precipitation is analysed in detail: first, the benefits brought about by the new setup are highlighted; subsequently, the equations are put in conservative hyperbolic form and the analytical recovery of the isopycnal model under $\kappa = 1$ is demonstrated. In section 3, the comparison of robust numerics with an adaptated analytical solution originally proposed by Shrira for nonlinear isopycnal shallow-water waves is shown as a numerical verification step, cf. (Shrira, 1981, 1986). In section 4, the full isentropic model endowed with convection and precipitation is outlined and a new (numerically simulated) nature run trajectory for future forecast-assimilation experiments is reported. Conclusions are provided in section 5.

2 An isentropic $1\frac{1}{2}$-layer shallow water model

2.1 Motivations

The development of a new, isentropic $1\frac{1}{2}$-layer shallow water model is motivated by the limitations posed by the single-layer *modRSW* model developed by Kent et al. (2017) in conducting idealized satellite data assimilation experiments. In this regard, the main issues are the lack of a robust physical definition of fluid temperature and the unrealistic scaling.
One way to proceed would be to equip the *modRSW* model with a simple diagnostic equation between the dimensionless fluid depth h and its dimensional temperature T based on the ideal gas law and hydrostatic equilibrium, such as:

$$T = T_0 h, \qquad \text{with} \quad T_0 = gH/R, \tag{2}$$

in which g is the acceleration due to gravity ($g = 9.81\,\mathrm{m\,s^{-2}}$) and H the scale height of the fluid. However, the scaling used in Kent et al. (2017) – i.e. $gH = 330\,\mathrm{m^2 s^{-2}}$, or $H \approx 34\,\mathrm{m}$ – is based on an unrealistic fluid depth H and leads to an unreasonable

scale temperature of $T_0 \simeq 1.1$ K. This configuration is clearly not suitable for satellite data assimilation purposes and highlights the need for a different approach.

In a paper by Pan and Smith (1999), an isopycnal $1\frac{1}{2}$-layer shallow water model is used to investigate gap winds and wakes in the presence of orography. Although the purpose of the study is different from ours, the fact that the authors used a shallow water model and based their scaling on real atmospheric observations makes this study attractive and interesting. Remarkably, despite the use of an isopycnal model, they employed the *isentropic* definition of the reduced gravity g', that is:

$$g' = \frac{\theta_1 - \theta_2}{\theta_1} g, \tag{3}$$

to compute the Froude number utilised in their numerical simulations. On the one hand, this combined use of an isopycnal model with the isentropic definition of the reduced gravity seems to guarantee a simple but realistic testbed for their numerical experiments. On the other hand, this choice cannot be seen as an entirely consistent one. It is precisely to remove this inconsistency that we decided to develop an entirely consistent $1\frac{1}{2}$-layer isentropic model. The *ismodRSW* model does not suffer from the scaling issues discussed above, and it is naturally equipped with a physically consistent temperature definition in terms of the potential temperature of each layer via eq. (1).

The scaling of the *ismodRSW* model used in this paper is discussed extensively in part II, as it is inherently linked to its analytical derivation as a reduced 2-layer model. Here it suffices to say that the scenario presented in this article is based on radiosonde data during a low-level jet (LLJ) event and therefore representative of real atmospheric conditions. The values of the scale variables used in this study are summarised in Table 1.

On a further note, the transition from a single to a $1\frac{1}{2}$-layer model offers additional benefits for the modelling of idealized satellite observations. Real satellite observations are radiance measurements shaped by several processes (emission, absorption and scattering) taking place throughout the atmosphere before the radiance reaches the satellite. In this sense, the degree of vertical complexity with which the atmosphere can be modelled plays a crucial role in mimicking the most relevant features of real satellite observations.

2.2 $1\frac{1}{2}$-layer isentropic shallow water

In part II we derive an asymptotically consistent $1\frac{1}{2}$-layer shallow water model in which an isentropic shallow layer of fluid at potential temperature θ_2 lies below a second (relatively) motionless layer at θ_1 ($\theta_1 > \theta_2$) capped by a rigid lid. A sketch if this model is given in Figure 1. The non-dimensional closed set of equations for such a system reads:

$$\partial_t \sigma_2 + \nabla \cdot (\sigma_2 \mathbf{v}_2) = 0, \tag{4a}$$
$$\partial_t \mathbf{v}_2 + (\mathbf{v}_2 \cdot \nabla)\mathbf{v}_2 + f \mathbf{v}_2{}^{\perp} = -\nabla M_2, \tag{4b}$$
$$M_1 = 0 \qquad \text{and} \qquad \mathbf{v}_1 = 0; \tag{4c}$$

in which: σ_2 is the pseudo-density in the bottom layer defined as:

$$\sigma_2 = \frac{p_r}{g}(\eta_2 - \eta_1); \tag{5}$$

$\mathbf{v}_i = (u_i, v_i)$ represents the velocity vector in the i-th layer and $\mathbf{v}_2^{\perp} = (-v_2, u_2)$ its perpendicular component in the lower layer; f is the Coriolis frequency; M_i is the Montgomery potential of each layer. The Montgomery potential M_2 in (4b) is defined as:

$$M_2 = c_p \theta_2 \eta_2{}^{\kappa} + g b, \tag{6}$$

with b representing the bottom topography. The depth of each layer is calculated as:

$$h_1 = (c_p \theta_1 / g)(\eta_1^{\kappa} - \eta_0^{\kappa}); \tag{7a}$$
$$h_2 = (c_p \theta_2 / g)(\eta_2^{\kappa} - \eta_1^{\kappa}). \tag{7b}$$

For the purpose of this paper, we apply two simplifications to the system above: (i) we assume flat bottom conditions (i.e. $b = 0$ in (6)) and (ii) flow independence of the meridional direction (i.e. $\partial_y = 0$). Given these two assumptions, the equations for (σ_2, u_2, v_2) read as:

$$\partial_t \sigma_2 + \partial_x (\sigma_2 u_2) = 0, \tag{8a}$$
$$\partial_t u_2 + u_2 \partial_x u_2 - f v_2 = -\partial_x M_2, \tag{8b}$$
$$\partial_t v_2 + u_2 \partial_x v_2 + f u_2 = 0. \tag{8c}$$

The system of equations (8) is closed since the non-dimensional pressure η_2 in (6) is linked to the pseudo-density σ_2 via its definition (5), with η_1 being

$$\eta_1 = \left[\frac{\theta_2}{\triangle\theta}\left(-\eta_2^\kappa + \frac{\theta_1}{\theta_2}\eta_0^\kappa + \frac{g}{c_p\theta_2}Z_0\right)\right]^{\frac{1}{\kappa}}, \tag{9}$$

in which η_0 is the (constant) non-dimensional pressure acting on the upper lid, $\Delta\theta = \theta_1 - \theta_2$ is the difference in potential temperature between the layers and $Z_0 = h_1 + h_2$ represents the total depth of the fluid. The derivation of equation (9) is detailed in Appendix A. A typical function relating σ_2 to η_2 for the scale variables reported in Table 1 is shown in Fig 2.

2.3 The conservative hyperbolic system

The numerical implementation of the nonlinear hyperbolic system (8) can be facilitated when it is written in the following conservative form:

$$\partial_t \mathbf{U} + \partial_x \mathbf{F}(\mathbf{U}) + \mathbf{T}(\mathbf{U}) = 0. \tag{10}$$

In order to write the system (8a-8c) in conservative form, we start by multiplying (8b) and (8c) by σ_2. Replacing M_2 in the momentum equation with (6) and after some manipulation (after dropping the subscripts for σ, u, v and η), we obtain:

$$\partial_t \sigma + \partial_x(\sigma u) = 0, \tag{11a}$$

$$\partial_t(\sigma u) + \partial_x\left(\sigma u^2\right) - f\sigma v = -c_p\theta_2\sigma\partial_x(\eta^\kappa), \tag{11b}$$

$$\partial_t(\sigma v) + \partial_x(\sigma u v) + f\sigma u = 0. \tag{11c}$$

The right-hand-side of eq. (11b) can be rewritten as the composite derivative of an unknown function $\mathcal{E}(\eta(x,t))$:

$$-\partial_x\mathcal{E}(\eta(x,t)) = -\partial_\eta\mathcal{E}\partial_x\eta \quad \text{with} \quad \frac{\partial\mathcal{E}}{\partial\eta} = \kappa c_p\theta_2\sigma(\eta)\eta^{\kappa-1}, \tag{12}$$

in which the analytical expression of the pseudo-density σ as a function of η reads (after substituting (9) into (5) and dropping the subscript in η_2):

$$\sigma(\eta) = \frac{p_r}{g}\left\{\eta - \left[\frac{\theta_2}{\triangle\theta}\left(-\eta^\kappa + \frac{\theta_1}{\theta_2}\eta_0^\kappa + \frac{g}{c_p\theta_2}Z_0\right)\right]^{\frac{1}{\kappa}}\right\}. \tag{13}$$

Integration of (12) with (13) yields:

$$\begin{aligned}\mathcal{E}(\eta) = c_p\theta_2\frac{p_r}{g}\frac{\kappa}{\kappa+1}\Bigg[&\eta^{\kappa+1} + \left(\frac{\theta_2}{\triangle\theta}\right)^{\frac{1}{\kappa}}\left(\frac{\theta_1}{\theta_2}\eta_0^\kappa + \frac{g}{c_p\theta_2}Z_0 - \eta^\kappa\right)^{\frac{\kappa+1}{\kappa}} + \\ &- \left(\frac{\theta_2}{\triangle\theta}\right)^{\frac{1}{\kappa}}\left(\frac{\theta_1}{\theta_2}\eta_0^\kappa + \frac{g}{c_p\theta_2}Z_0\right)^{\frac{\kappa+1}{\kappa}}\Bigg].\end{aligned} \tag{14}$$

Therefore, the momentum equation can be expressed as:

$$\partial_t(\sigma u) + \partial_x\left(\sigma u^2 + \mathcal{E}\right) - f\sigma v = 0, \tag{15}$$

and system (11) can be written in conservative form (10) with $\mathbf{U}$, $\mathbf{E}(\mathbf{U})$ and $\mathbf{T}(\mathbf{U})$ defined as follows:

$$\mathbf{U} = \begin{pmatrix}\sigma\\ \sigma u\\ \sigma v\end{pmatrix}, \quad \mathbf{F}(\mathbf{U}) = \begin{pmatrix}\sigma u\\ \sigma u^2 + \mathcal{E}\\ \sigma u v\end{pmatrix}, \quad \mathbf{T}(\mathbf{U}) = \begin{pmatrix}0\\ -f\sigma v\\ f\sigma u\end{pmatrix}. \tag{16}$$

By writing $\sigma u^2 = (\sigma u)^2/\sigma$ and $\sigma uv = (\sigma u)(\sigma v)/\sigma$, the Jacobian of the system reads as:

$$\mathbf{J}(\mathbf{U}) \equiv \partial_{\mathbf{U}}\mathbf{F} = \begin{pmatrix}0 & 1 & 0\\ -u^2 + \partial_\sigma\mathcal{E} & 2u & 0\\ -uv & v & u\end{pmatrix}, \tag{17}$$

with eigenvalues:

$$\lambda_{1,2} = u \pm \sqrt{\partial_\sigma\mathcal{E}} \quad \text{and} \quad \lambda_3 = u. \tag{18}$$

Here, $\partial_\sigma \mathcal{E}$ is computed to be:

$$\frac{\partial}{\partial \eta}\mathcal{E}\left(\sigma\left(\eta\right)\right) = \frac{\partial \mathcal{E}}{\partial \sigma}\frac{\mathrm{d}\sigma}{\mathrm{d}\eta} \Longrightarrow \frac{\partial \mathcal{E}}{\partial \sigma} = \frac{\frac{\partial \mathcal{E}}{\partial \eta}}{\frac{\mathrm{d}\sigma}{\mathrm{d}\eta}} = \frac{\kappa c_p \theta_2 \sigma\left(\eta\right)\eta^{\kappa-1}}{\frac{\mathrm{d}\sigma}{\mathrm{d}\eta}}, \tag{19}$$

after using (12) in the numerator and with denominator:

$$\frac{\mathrm{d}\sigma}{\mathrm{d}\eta} = \frac{p_r}{g}\left[1+\left(\frac{\theta_2}{\triangle\theta}\right)^{1/\kappa}\left(\frac{\theta_1}{\theta_2}\eta_0^\kappa + \frac{g}{c_p\theta_2}Z_0 - \eta^\kappa\right)^{(1-\kappa)/\kappa}\eta^{\kappa-1}\right]. \tag{20}$$

A plot of $\partial\mathcal{E}/\partial\sigma$ in Fig. 3 shows that it is positive for non-negative values of σ, also confirming the hyperbolic character of system (11), with real and distinct eigenvalues λ in (18) for $\partial_\sigma\mathcal{E} > 0$. The numerical scheme used to integrate the model can therefore be chosen to be close to the one in Kent et al. (2017) with minor adaptations. More details can be found in the Appendix B.

2.4 Recovery of the isopycnal model

We conclude this section by showing how the isentropic $1\frac{1}{2}$-layer shallow water model can be traced back to its isopycnal counterpart by taking $\kappa = 1$ in (1). Incidentally, this should help visualize the inconsistency of using the isentropic definition of the reduced gravity (3) within an isopycnal model, as we argued earlier.
Starting from (7b) with $\kappa = 1$, a linear relation between the fluid depth h_2 and non-dimensional pressure η_2 (and thus pseudo-density σ_2) is restored:

$$h_2 = \frac{c_p\theta_2}{g}\left(\eta_2 - \eta_1\right) = \frac{c_p\theta_2}{p_r}\sigma_2. \tag{21}$$

Substituting the above expression back into the continuity equation (8a) yields:

$$\partial_t h_2 + \partial_x\left(h_2\, u_2\right) = 0, \tag{22}$$

equivalent to the continuity equation of the isopycnal model. In addition, we observe that for $\kappa = 1$ the Montgomery potential M_2 in (8b) becomes:

$$M_2 = c_p\,\theta_2\,\eta_2.$$

By using (7) for $\kappa = 1$, we obtain:

$$c_p\theta_2\eta_2 = g h_2 + g h_1\theta_2/\theta_1 + c_p\theta_2\eta_0. \tag{23}$$

After using the rigid lid constraint $H = h_1 + h_2$ and substituting back into the Montgomery potential and the momentum equation (8b), we obtain the usual momentum equation for an isopycnal fluid:

$$\partial_t u_2 + u_2\partial_x u_2 - f\, v_2 = -g'\partial_x h_2, \tag{24}$$

with reduced gravity g' defined as in (3). However, since $\kappa = 1$ implies $\theta = T(p_r/p)$, we note that:

$$\frac{\theta_1-\theta_2}{\theta_1} = \frac{T_1/p_1 - T_2/p_2}{T_1/p_1} = \frac{1/\rho_1 - 1/\rho_2}{1/\rho_1} = \frac{\rho_2-\rho_1}{\rho_2}, \tag{25}$$

making use of the ideal gas law ($p = \rho RT$). In other words, the isopycnal expression of the reduced gravity is recovered for $\kappa = 1$. The numerical convergence of the two models for $\kappa = 1$ will be used as a final check for the *ismodRSW* model in section 4c.

3 Shrira's solution for nonlinear waves

In this section we provide an independent analytical verification of the numerical model using an extended version of Shrira's analysis of stationary nonlinear waves propagating on the surface of a rotating isopycnal or shallow-water layer fluid (Shrira, 1981, 1986), adapted to our isentropic model. We start by splitting the pseudo-density σ into a state σ_0 and a perturbation $\tilde{\sigma}$:

$$\sigma = \sigma_0 + \tilde{\sigma} \quad \text{with} \quad \tilde{\sigma} = \frac{\sigma_0}{f}\frac{\partial v}{\partial x}. \tag{26}$$

The validity of (26) for $\tilde{\sigma}$ follows by substituting into the continuity equation (11a) and using the meridional momentum equation, obtaining the identity:

$$\frac{\sigma_0}{f}\frac{\partial^2 v}{\partial x \partial t} + \frac{\partial}{\partial x}\left[\left(\sigma_0 + \frac{\sigma_0}{f}\frac{\partial v}{\partial x}\right)u\right] = 0,$$
$$\frac{\partial}{\partial x}\left[\frac{\partial v}{\partial t} + fu + u\frac{\partial v}{\partial x}\right] = 0 \quad \Longrightarrow \quad 0 = 0.$$

Using (8c) to express u as a function of $\frac{\partial v}{\partial x}$ and $\frac{\partial v}{\partial t}$, one finds (assuming $\frac{\partial v}{\partial x} + f \neq 0$):

$$u = -\frac{\partial v}{\partial t}/(\frac{\partial v}{\partial x} + f). \tag{27}$$

Differentiating (8c) by t and using both (8b) and (27), yields:

$$\frac{\partial^2 v}{\partial t^2} + f^2 v - f\frac{\partial M}{\partial x} = \frac{\partial}{\partial t}\left(\frac{\frac{\partial v}{\partial x}\frac{\partial v}{\partial t}}{f + \frac{\partial v}{\partial x}}\right) + \frac{f}{2}\frac{\partial}{\partial x}\left(\frac{\left(\frac{\partial v}{\partial t}\right)^2}{\left(f + \frac{\partial v}{\partial x}\right)^2}\right), \tag{28}$$

resembling Eq. (10) in Shrira (1981) and Eq. (4) in Shrira (1986) (once y–derivatives are dropped in the older paper and the high-frequency dispersion term is neglected).
The gradient of the Montgomery potential becomes:

$$\frac{\partial}{\partial x}M(\eta(\sigma)) = \frac{\partial M}{\partial \eta}\frac{\mathrm{d}\eta}{\mathrm{d}\sigma}\frac{\partial \sigma}{\partial x} = c_p \theta \kappa \eta^{\kappa-1}\left(\frac{1}{\frac{\mathrm{d}\sigma}{\mathrm{d}\eta}}\right)\frac{\sigma_0}{f}\frac{\partial^2 v}{\partial x^2}, \tag{29}$$

after using σ' from (26). Substituting (29) into (28) gives:

$$\frac{\partial^2 v}{\partial t^2} + f^2 v - f c_p \theta \kappa \eta^{\kappa-1}\left(\frac{1}{\frac{\mathrm{d}\sigma}{\mathrm{d}\eta}}\right)\frac{\sigma_0}{f}\frac{\partial^2 v}{\partial x^2} = \frac{\partial}{\partial t}\left(\frac{\frac{\partial v}{\partial x}\frac{\partial v}{\partial t}}{f + \frac{\partial v}{\partial x}}\right) + \frac{f}{2}\frac{\partial}{\partial x}\left(\frac{\left(\frac{\partial v}{\partial t}\right)^2}{\left(f + \frac{\partial v}{\partial x}\right)^2}\right).$$

For travelling waves of phase velocity c, we define $\zeta = x - ct$ and rewrite the equation above, with primes denoting $\frac{\partial}{\partial \zeta}$, to obtain a 2^{nd}–order ODE in ζ:

$$c^2 v'' + f^2 v - f c_p \theta \kappa \eta^{\kappa-1}\left(\frac{1}{\frac{\mathrm{d}\sigma}{\mathrm{d}\eta}}\right)\frac{\sigma_0}{f}v'' = c^2\left(\frac{(v')^2}{f + v'}\right)' + \frac{f c^2}{2}\left(\frac{(v')^2}{(f+v')^2}\right)'. \tag{30}$$

After some manipulation, one finds

$$v'' = \frac{\frac{f^2}{c^2}v}{\frac{f}{c^2}c_p \theta \kappa \eta^{\kappa-1}\left(\frac{1}{\frac{\mathrm{d}\sigma}{\mathrm{d}\eta}}\right)\frac{\sigma_0}{f} - \frac{f^3}{(f+v')^3}},$$

non-dimensionalized as follows:

$$\mathrm{v}'' = \frac{1}{\mathrm{Ro}^2}\frac{\mathrm{v}}{\frac{c_p \theta}{c^2}\kappa \eta^{\kappa-1}\left(\frac{1}{\frac{\mathrm{d}\sigma}{\mathrm{d}\eta}}\right)\sigma_0 - \frac{1}{\mathrm{Ro}^3}\frac{1}{\left(\frac{1}{\mathrm{Ro}} + \mathrm{v}'\right)^3}}, \tag{31}$$

using $v = c\mathrm{v}$, $\mathrm{Ro} = c/fL$ and $(\cdot)' = \frac{\partial}{\partial \zeta} = \frac{1}{L}\frac{\partial}{\partial \zeta'} = \frac{1}{L}(\cdot)'$. This ODE is solved with a Runge-Kutta $4^{'th}$–order method after rewriting it as follows:

$$\chi = \mathrm{v}', \quad \chi' = F(\chi, \mathrm{v}, \zeta) = \frac{\frac{1}{\mathrm{Ro}^2}\mathrm{v}}{\left[-\frac{1}{\mathrm{Ro}^3}\frac{1}{\left(\frac{1}{\mathrm{Ro}} + \chi\right)^3} + \widetilde{c_p}\theta \kappa \eta^{\kappa-1}\left(\frac{1}{\frac{\mathrm{d}\sigma}{\mathrm{d}\eta}}\right)\sigma_0\right]}, \tag{32}$$

with $\widetilde{c_p} = c_p/c^2$. For comparison with the full model (11), we derive the expressions also for the (non-dimensional) u and $\bar{\sigma}$, using (27) and (26), and scaling u and σ_0 by c and g/p_r, respectively:

$$\mathrm{u} = \chi/(1/\mathrm{Ro} + \chi) \quad \text{and} \quad \bar{\sigma} = \sigma_0(1 + \mathrm{Ro}\chi). \tag{33}$$

The solution of (32) is stable only within a certain range of initial conditions for v_0 and χ_0. Once a stable configuration is found, the phase velocity c is tuned in order to obtain a single-wavelength wave in v, u and $\bar{\sigma}$ as solution and subsequently used as initial condition for the isentropic $1\frac{1}{2}$-layer model. A comparison between Shira's solution and its numerical implementation at various times t and up to $t = 10\mathrm{T}$ periods is shown in Figure 4. Although the dissipative character of the numerical scheme used in this paper contributes to both an amplitude and a phase error as time goes by, the numerical solution (purple to red solid lines) visually converges towards the analytical one (gray line) as the resolution increases.

4 Modified isentropic $1\frac{1}{2}$-layer model

4.1 Adding convection and rain

In this section, we extend the rotating isentropic $1\frac{1}{2}$-layer model so that it mimics convection and precipitation in a similar manner to the isopcynal *modRSW* model. Hence, a system of thresholds is introduced in addition to an equation for the (dimensionless) rain mass fraction r, as follows:

$$\partial_t \sigma + \partial_x(\sigma u) = 0, \tag{34a}$$

$$\partial_t(\sigma u) + \partial_x(\sigma u^2 + \widetilde{\mathcal{E}}) + \sigma c_0^2 \partial_x r - f\sigma v = 0, \tag{34b}$$

$$\partial_t(\sigma v) + \partial_x(\sigma uv) + f\sigma u = 0, \tag{34c}$$

$$\partial_t(\sigma r) + \partial_x(\sigma ur) + \sigma\widetilde{\beta}\partial_x u + \alpha\sigma r = 0, \tag{34d}$$

where $\widetilde{\mathcal{M}}$ (playing the role of the effective pressure in Kent et al. (2017)) is defined as:

$$\widetilde{\mathcal{E}} = \begin{cases} \mathcal{E}(\sigma_c) & \text{for } \sigma > \sigma_c, \\ \mathcal{E}(\sigma) & \text{otherwise;} \end{cases} \tag{35}$$

with σ_c a convection threshold and:

$$\widetilde{\beta} = \begin{cases} \beta & \text{for } \sigma > \sigma_r \text{ and } \partial_x u < 0; \\ 0 & \text{otherwise;} \end{cases} \tag{36}$$

in which σ_r is a rain threshold. Parameters α (s^{-1}) and β (dimensionless) control the rate at which rain is created and removed from the system. The constant speed squared c_0^2 ($\mathrm{m}^{-2}\mathrm{s}^{-2}$) converts the dimensionless rain mass fraction into a potential, introducing a coupling between the two equations and implicitly controlling the suppression of convection, cf. Kent et al. (2017); Kent (2016).

Similarly to the *modRSW* model, the isentropic model endowed with convection and rain cannot be written in conservative form. Its intrinsic non-conservative vector formulation reads

$$\partial_t \mathbf{U} + \partial_x \mathbf{F}(\mathbf{U}) + \mathbf{G}(\mathbf{U})\partial_x \mathbf{U} + \mathbf{S}(\mathbf{U}) = 0, \tag{37}$$

where:

$$\begin{gathered} \mathbf{U} = \begin{pmatrix} \sigma \\ \sigma u \\ \sigma v \\ \sigma r \end{pmatrix}, \quad \mathbf{F}(\mathbf{U}) = \begin{pmatrix} \sigma u \\ \sigma u^2 + \widetilde{\mathcal{E}} \\ \sigma uv \\ \sigma ur \end{pmatrix}, \\ \mathbf{G}(\mathbf{U}) = \begin{pmatrix} 0 & 0 & 0 & 0 \\ -c_0^2 r & 0 & 0 & c_0^2 \\ 0 & 0 & 0 & 0 \\ -\widetilde{\beta}u & \widetilde{\beta} & 0 & 0 \end{pmatrix}, \quad \mathbf{S}(\mathbf{U}) = \begin{pmatrix} 0 \\ -f\sigma v \\ f\sigma u \\ \alpha\sigma r \end{pmatrix}. \end{gathered} \tag{38}$$

The Jacobian matrix $\mathbf{J} = \partial_{\mathbf{U}}\mathbf{F} + \mathbf{G}$ of the system reads:

$$\mathbf{J} = \begin{pmatrix} 0 & 1 & 0 & 0 \\ -u^2 - c_0^2 r + \partial_\sigma \widetilde{\mathcal{E}} & 2u & 0 & c_0^2 \\ -uv & v & u & 0 \\ -u(\widetilde{\beta} + r) & \widetilde{\beta} + r & 0 & u \end{pmatrix},$$

with eigenvalues:

$$\lambda_{1,2} = u \pm \sqrt{\partial_\sigma \widetilde{\mathcal{E}} + c_0^2 \widetilde{\beta}} \quad \text{and} \quad \lambda_{3,4} = u. \tag{39}$$

Again, the numerical discretization is an adaptation of the one in Kent et al. (2017). More details can be found in the Appendix B.

4.2 A new nature run for data assimilation

In Kent et al. (2020), we have demonstrated how the *modRSW* model is a viable tool to conduct data assimilation research for operational Numerical Weather Prediction (NWP). In particular, forecast-assimilation experiments have been conducted and subsequently analysed to show how the system, despite its idealizations, performs akin to operational DA schemes following a variety of metrics and criteria. In Kent et al. (2020), a so-called twin-setting configuration was used, in which observations are obtained from a high-resolution deterministic run, i.e. *nature run* or simulation, whereas the background state is generated by running the model at a lower resolution. Similarly, to conduct new satellite data assimilation experiments for our novel *ismodRSW* model, it is essential to find a dynamically interesting nature run, characterized by a continuous production of convection and precipitation. The absence of topography in the new configuration complicates the task somewhat since the presence of topography in a periodic domain with a zonal flow constituted a convenient setup to obtain self-generation of gravity waves in Kent et al. (2020).

To compensate for the absence of topography, both rotation and a forcing term were introduced, with the latter consisting of a relaxation term in the meridional momentum equation:

$$\partial_t v + u\partial_x v + fu = (v_{rel} - v)/\tau_{rel}, \tag{40}$$

in which τ_{rel} is a relaxation time-scale defining the speed at which the meridional velocity v relaxes towards $v_{rel}(x,t)$. The relaxation profile v_{rel} is shown in Fig. 5 (blue line) and represents a smoothed top-hat meridional jet. This type of forcing is chosen to reflect the troposphere-based scaling used in the derivation of the *ismodRSW* model in part II (cf. section §4b therein), which is based on Low Level Jet (LLJ) conditions (here approximated by a transverse jet in the meridional direction) in a 2-layer troposphere. The initial condition used in the nature run is also shown in Fig. 5 (red lines). In this case, the shape of both the pseudo-density profile and the meridional velocity simply represents an unstable setup that maximize the production of convection and rain at the beginning of the simulation. Finally, in Table 2 we list the parameter set used in the *ismodRSW* model to generate a 48 hours-long nature run with continuous production of rain and precipitation. The dynamical evolution of the nature run is shown in Hovmöller diagrams, one for each variable, in Fig. 6. The two top panels (right: σ, left: r) show how convection and rain are continuously generated across the (periodic) domain, as travelling waves move along it. Grey-shaded areas in the top-left panel indicate locations where only convection is activated ($\sigma_c < \sigma < \sigma_r$), whereas yellow-to-brown shadings denote areas of rain production ($\sigma > \sigma_r$). The fluid velocities are depicted in the bottom two panels (left: u, right: v). Areas of rain in the top right panel are spatially correlated with areas where convergence in u arises, e.g. at locations where a negative gradient of u exists. The Hovmöller diagram of the meridional velocity v (bottom-right panel) shows a much smoother time evolution than the other three variables as it shows the transition from the initial condition towards the relaxation solution.

The unsettled character of the nature run is further illustrated in Fig. 7, where the time series of all variables at location $x_0 = 0.5$ are shown. The peaks and troughs in the pseudo-density $\sigma(x_0)$ indicate the passage of the gravity waves at this location, with corresponding generation and removal of rain $r(x_0)$. The transit of waves is also correlated with some irregular oscillations in the horizontal velocity $u(x_0)$, while the meridional velocity $v(x_0)$, initially zero, gradually settles towards its relaxation solution v_{rel}, that is, a jet at the center of the domain (cf. Fig. 5).

4.3 Recovery of the *modRSW* model in presence of convection and rain

As a final check performed on the full model, we compare the evolution in time of the *modRSW* against the *ismodRSW* model with $\kappa = 1$. The two models are initialized with the same initial condition and the parameters reported in Table 2. The initial values of the fluid depth H_0, and the related thresholds H_c and H_r are scaled to $H_0 = 1$, $H_c = \sigma_c/\sigma_0 = 1.05$ and $H_r = \sigma_r/\sigma_0 = 1.2$ with $\sigma_0 = 0.2$ (see Table 2 and Fig. 5). The value of Froude number in the bottom layer Fr_2 (which needs to be specified in the *modRSW* model) is reported in Table 2 and is computed as:

$$\mathrm{Fr}_2 = \frac{U_2}{\sqrt{g' h_2}} = \frac{U_2}{\sqrt{g \frac{\Delta\theta}{\theta_1} \frac{R\theta_2}{g} \frac{g}{p_r} \sigma}}, \tag{41}$$

in which we have used the definition of the isentropic reduced gravity g' in (3), the expression of the bottom layer depth h_2 in (7b) and the definition of σ in (13).

We run the two models side-by-side in three different configurations: (i) classic rotating shallow water ($\sigma_c, \sigma_r \to \infty$), (ii) convection-only regime ($\sigma_r \to \infty$) and (iii) fully modified shallow water. The results (limited to h, σ and r) are shown in Figure 8. While in the first two cases (left and central panels) the two models behave identically (we notice the good agreement between the solid black for h and the dashed gray line for σ in the left and central panels), we observe a gradual divergence in time between the two once both convection and rain are turned on (right panels, after $t = 0.75$). The differences are particularly noticeable in the rain solutions (blue solid and cyan dashed lines). This divergence seems to originate (and grow thereafter) at various locations in the domain where σ (and similarly h) decreases until it falls below the rain threshold. We believe this is an indirect effect of rounding errors generated by the computation of the different flux expressions in the two models (cf. eq. (38) in this article with eq. (6) in Kent et al. (2017)), which in turn has an impact on the values of the non-conservative products. After all, this type of behaviour is not surprising given the non-linear character of the two models.

5 Conclusions and future work

Satellite data are used extensively in data assimilation for NWP models. Their inclusion in operational systems dates back to the 1970s (Eyre et al., 2020) and represented a crucial step in a decades-long effort towards more accurate weather forecasting, with active research on how to make the best use of them continuing today. To this aim, a variety of simplified and idealized models are sometimes used, especially when the high degree of complexity and the big computational power typical of data assimilation schemes would hamper the success and the efficacy of the research on this subject.

In this paper, we presented a novel $1\frac{1}{2}$-layer isentropic model based on modified isopycnal-layer equations (*ismodRSW*) which will be used for satellite data assimilation research. A companion paper (part II) covers the formal analytical derivation of this model without convection and precipitation.

The *ismodRSW* model represents an upgrade of the *modRSW* model ((Kent, 2016; Kent et al., 2017)) in which a single-layer of fluid at constant density is replaced by two layers at constant potential temperature capped by a rigid lid. The new model is able to mimic convection and precipitation by retaining the same threshold mechanism already in place in the *modRSW* model. The necessity for a model revision has been motivated by two limitations of the original model: the lack of vertical structure in the single-layer configuration and the difficulties found in defining a diagnostic relationship for temperature, cf. §22.1. Both these aspects hampered the possibility of performing meaningful satellite data assimilation experiments with the *modRSW* model. Our new *ismodRSW* model addresses those limitations, providing both a robust temperature definition within each layer and a multi-layer dynamics restricted to a $1\frac{1}{2}$-layer configuration.

In this paper we provide two checks on the numerical implementation of our new model: on the one hand, we have successfully compared the numerical model (without convection and precipitation) against an analytical solution for stationary waves adapted from Shrira (1981, 1986), cf. §3. Moreover, we demonstrated that the isopycnal model can be recovered from the isentropic for $\kappa = R/c_p = 1$. This was verified numerically by running the old and the new model side-by-side for the same physical scaling, boundary and initial conditions. Results were identical except in the presence of both convection and rain, where small rounding errors eventually led to divergence of the two model trajectories, implicitly confirming the high non-linearity of the system with its switches (see §4c).

The *ismodRSW* model will be used to conduct idealized satellite data assimilation experiments with an Ensemble Kalman Filter in a twin setting configuration (cf. section 6.1 of Kent (2016); Kent et al. (2020)). The model will be run at two different resolutions with the observations to be derived from a deterministic high-resolution simulation (constituting the 'truth' model trajectory, or nature run), and the low-resolution simulations treated as the forecasts. In this regard, we showed in section 4 that continuous creation and propagation of gravity waves (essential to recreate an interesting model dynamics) can be achieved with the *ismodRSW* model by exploiting rotation and relaxation to a given v_{rel} solution in a periodic domain, paving the way for new forecast-assimilation experiments relevant for satellite data assimilation research. Another (although unexplored) option would have been to exploit the analytical Shrira's solution discussed earlier which could have the potential to trigger traveling gravity waves with generation of convection and rain; even in that case, a relaxation solution might be needed to counteract the dissipation given by the numerical scheme.

In particular, the focus of future research will be on investigating the role of satellite observations at different spatial scales, understanding what has a greater impact: whether focusing on the large-synoptic scale or, rather, the convective small-scale features. Herein, the development of a new, nonlinear observation operator (with respect to the linear one used in Kent et al. (2020)) will be crucial. The new model will be particularly helpful, since pseudo-observations of radiance can be simulated with the help of a radiative scheme, now that a well–defined and more realistic relationship between one of the prognostic variables (in this case σ) and the layer temperature exists. Moreover, although two layers are not enough to replicate satellite weighting functions, they can be used to produce vertically integrated pseudo-observations, with weighted contributions from each layer, depending on their temperature and other (layer-dependent) radiative properties. The possibility of modeling clouds can also be taken into account by making the observation operator more elaborate: for example, convection and the rain thresholds can be used to define 'non-precipitating' and 'precipitating' clouds.

Acknowledgments

This work stems from the work done by Luca Cantarello under a NERC SPHERES DTP scolarship (NE/L002574/1, reference 1925512), co-funded by the Met Office via a CASE partnership. We thank Gordon Inverarity (Met Office) for his useful comments on an earlier draft. We do not have conflicts of interest to disclose.

Appendices

A Derivation of the expression for η_1

In this appendix we show how to derive the expression for the dimensionless pressure η_1 in equation (9). The starting point is represented by equation (23) in Bokhove and Oliver (2009), which in the case of a 2-layer model reads (i.e. $N = 2$, $\alpha = \beta = 1$):

$$M_1 = M_2 + c_p \Delta\theta \eta_1^\kappa. \tag{A1}$$

As suggested in the same paper, a constant of integration $c = -(c_p \theta_1 \eta_0^\kappa + gZ_0)$ can be added to the equation above when imposing a rigid-lid boundary condition (leading to a $1\frac{1}{2}$-layer model):

$$M_1 = M_2 + c_p \Delta\theta \eta_1^\kappa - (c_p \theta_1 \eta_0^\kappa + gZ_0). \tag{A2}$$

Substituting (6) in the above expression gives:

$$M_1 = c_p \theta_2 \eta_2^\kappa + gb + c_p \Delta\theta \eta_1^\kappa - (c_p \theta_1 \eta_0^\kappa + gZ_0). \tag{A3}$$

The expression for η_1 is therefore obtained by imposing $M_1 = 0$ in (A3) in virtue of (4c) and by rearranging it appropriately (with $b = 0$ in the case of flat topography).

B Numerical scheme for the *ismodRSW* model

In this appendix we summarize the numerical methods utilised to integrate the *ismodRSW* model. Despite some modifications, the scheme has remained the same used in Kent (2016); Kent et al. (2017), which we refer the reader to for a more comprehensive and satisfactory description.

B.1 Classic shallow water

To integrate numerically the model in absence of convection and rain (i.e. the 1.5-layer isentropic shallow water model illustrated in sections §2 and §3), a 0-degree discretization of the Discontinuous Galerkin Finite Element Method (DGFEM) developed by Rhebergen et al. (2008) is used, in combination with HLL fluxes (Harten et al., 1983). As we saw in section §22.3, the shallow water model is hyperbolic and can be put in conservative form.
We split the horizontal domain $[0, L]$ into N open elements $K_k = (x_k, x_{k+1})$ of constant length $|K_k| = x_{k+1} - x_k$ with $k = 1, 2, ..., N_{el}$, delimited by $N_{el} + 1$ nodes where $0 = x_1, x_2, ..., x_N, x_{N_{el}+1} = L$. Therefore, we derive the weak formulation of equation (10) (see §3.1.2 of Kent (2016) and more extensively Zienkiewicz et al. (2014)). The zero-degree discretization (henceforth DG-0) implies that the function $\mathbf{U}$ in (10) is approximated with a piece-wise constant function within each element K_k such as:

$$\mathbf{U}_h(x,t) = \overline{U}_k = \frac{1}{|K_k|} \int_{K_k} \mathbf{U}(x,t) dx. \tag{B1}$$

In the end, the DG-0 discretization for each element $|K_k|$ reads:

$$\frac{\mathrm{d}\overline{U}_k}{\mathrm{d}t} + \frac{\mathcal{F}_{k+1} - \mathcal{F}_k}{|K_k|} + T(\overline{U}_k) = 0, \tag{B2}$$

where $\mathcal{F}_k$ represents the numerical flux computed at each element's node, which for the HLL fluxes is defined as:

$$\mathcal{F}_k = \begin{cases} F^L & \text{if } S^L > 0, \\ F^R & \text{if } S^R < 0, \\ F^{HLL} & \text{if } S^L < 0 < S^R, \end{cases} \tag{B3}$$

with F^{HLL} defined as:

$$F_i{}^{HLL} = \frac{F_i{}^L S^R - F_i{}^R S^L + S^L S^R (U_i{}^R - U_i{}^L)}{S^R - S^L}, \tag{B4}$$

in which S^L and S^R are the numerical velocities arising from the eigenvalues in Eq. (18):

$$S^L = \min\left(u_k - \sqrt{\partial_\sigma \mathcal{M}_k},\, u_{k+1} - \sqrt{\partial_\sigma \mathcal{M}_{k+1}}\right); \tag{B5a}$$

$$S^R = \max\left(u_k + \sqrt{\partial_\sigma \mathcal{M}_k},\, u_{k+1} + \sqrt{\partial_\sigma \mathcal{M}_{k+1}}\right). \tag{B5b}$$

It is worth noticing that in order to compute the fluxes $\mathcal{F}$ and the numerical velocities S^L, S^R, the non-dimensional pressure η needs to be calculated at each time step from the pseudo-density σ. However, since inverting analytically eq. (5) is not possible, an alternative which is efficient enough needs to be found. Here we chose to precompute the corresponding values of σ and η (with a resolution of $\delta\sigma = 0.0001$) and to perform a linear interpolation during the model integration. A polynomial interpolation is also possible.
We refer to Kent (2016) for the (adaptive) time step implementation.

B.2 NCPs for the full model

We noted in section 4 that the model in its full form - comprising convection and rain - cannot be put in conservative form, and that non-conservative products arise and need to be handled numerically (see eq. (37)). To this aim, nonwithstanding the DGFEM method outlined above, the DLM theory introduced by Dal Maso et al. (1995) is used. Again, more details about the mathematical formulation of this scheme can be found in Kent (2016) and Kent et al. (2017), although in this case (beacuse of the missing topography term) there is no need to apply the theory about state reconstruction used therein and the scheme developed by Audusse et al. (2004).
The following semi-discrete space-DGFEM scheme for a single element K_k is found:

$$\frac{\mathrm{d}\overline{U}_k}{\mathrm{d}t} + \frac{\mathcal{P}^p_{k+1} - \mathcal{P}^m_k}{|K_k|} + S(\overline{U}_k) = 0, \tag{B6}$$

in which the numerical fluxes $\mathcal{P}^p_i$ and $\mathcal{P}^m_i$ read as:

$$\mathcal{P}^p_i = \mathcal{P}^{NC}_i + \frac{1}{2}\int_0^1 G_{ij}(\boldsymbol{\phi})\frac{\partial \phi_j}{\partial \tau} d\tau, \tag{B7}$$

$$\mathcal{P}^m_i = \mathcal{P}^{NC}_i - \frac{1}{2}\int_0^1 G_{ij}(\boldsymbol{\phi})\frac{\partial \phi_j}{\partial \tau} d\tau. \tag{B8}$$

In the expressions above, $G_{ij}(\boldsymbol{\phi})$ indicates the $\{i, j\}$ matrix element of the NCP $\mathbf{G}$ matrix of eq. (38), with $\boldsymbol{\phi}$ being a Lipschitz continuous path connecting the left and the right state: $\boldsymbol{\phi}(\tau; \mathbf{U}^L, \mathbf{U}^R) = \mathbf{U}^L + \tau\left(\mathbf{U}^R - \mathbf{U}^L\right)$, as per the DLM theory. Moreover, the NCP flux contributions $\mathcal{P}^{NC}_i$ read as:

$$\mathcal{P}^{NC}_i(\overline{U}^L_i, \overline{U}^R_i) = \begin{cases} F^L_i - \frac{1}{2}V^{NC}_i, & \text{if } S^L > 0; \\ F^{HLL}_i - \frac{1}{2}\frac{S^L + S^R}{S^R - S^L}V^{NC}_i, & \text{if } S^L < 0 < S^R; \\ F^R_i + \frac{1}{2}V^{NC}_i, & \text{if } S^R < 0. \end{cases} \tag{B9}$$

with the numerical velocities S^L and S^R (cf. eq. (39)) being:

$$S^L = \min\left(u^L - \sqrt{\partial_\sigma \mathcal{M}|^L + c_0^2\widetilde{\beta}|^L}, u^R - \sqrt{\partial_\sigma \mathcal{M}|^R + c_0^2\widetilde{\beta}|^R}\right), \tag{B10}$$

$$S^R = \max\left(u^L + \sqrt{\partial_\sigma \mathcal{M}|^L + c_0^2\widetilde{\beta}|^L}, u^R + \sqrt{\partial_\sigma \mathcal{M}|^R + c_0^2\widetilde{\beta}|^R}\right). \tag{B11}$$

$\mathbf{V}^{NC}$ is a vector containing the worked out contribution of the NCP integral expressions $\int_0^1 G_{ij}(\boldsymbol{\phi})\frac{\partial \phi_j}{\partial \tau} d\tau$:

$$\mathbf{V}^{NC} = \begin{bmatrix} 0 \\ -c_0^2[[r]]\{\{\sigma\}\} \\ 0 \\ -\beta[[u]]\Theta([[u]])\left(\sigma^R I_\beta + [[\sigma]]I_{\tau\beta}\right) \end{bmatrix}, \tag{B12}$$

where: $\Theta(\cdot)$ indicates the Heaviside function, $[[\cdot]] = (\cdot)^L - (\cdot)^R$ the jump across the node and $\{\{\cdot\}\} = \frac{1}{2}\left((\cdot)^L + (\cdot)^R\right)$ the average quantity. I_β and $I_{\tau\beta}$ are still expressed by eqs. (C18) and (C22) as per appendix C of Kent et al. (2017), with analogous derivation upon the redefinition of X and Y as $X = \sigma^R - \sigma^L$ and $Y = \sigma^L - \sigma_r$. The derivations of the elements in $\mathbf{V}^{NC}$ is also analogous to the one performed in the same appendix, by replacing all references to z and h with σ.

References

Audusse, E., F. Bouchut, M.-O. Bristeau, R. Klein, and B. t. Perthame, 2004: A fast and stable well-balanced scheme with hydrostatic reconstruction for shallow water flows. *SIAM Journal on Scientific Computing*, **25 (6)**, 2050–2065.

Bannister, R. N., 2020: The ABC-DA system (v1. 4): a variational data assimilation system for convective scale assimilation research with a study of the impact of a balance constraint. *Geoscientific Model Development Discussions*, 1–42.

Bokhove, O., L. Cantarello, and S. Tobias, 2021: An idealized $1\frac{1}{2}$-layer isentropic model with convection and precipitation for satellite data assimilation research. Part II: model derivation.

Bokhove, O., and M. Oliver, 2009: A parcel formulation of hamiltonian layer models. *Geophys. Astrophys. Fluid Dyn*, **103 (6)**, 423–442.

Dal Maso, G., P. G. Lefloch, and F. Murat, 1995: Definition and weak stability of nonconservative products. *Journal de mathématiques pures et appliquées*, **74 (6)**, 483–548.

Ehrendorfer, M., and R. M. Errico, 2008: An atmospheric model of intermediate complexity for data assimilation studies. *Quarterly Journal of the Royal Meteorological Society*, **134 (636)**, 1717–1732.

Eyre, J. R., S. J. English, and M. Forsythe, 2020: Assimilation of satellite data in numerical weather prediction. part i: The early years. *Quarterly Journal of the Royal Meteorological Society*, **146 (726)**, 49–68.

Geer, A., and Coauthors, 2017: The growing impact of satellite observations sensitive to humidity, cloud and precipitation. *Quarterly Journal of the Royal Meteorological Society*, **143 (709)**, 3189–3206.

Geer, A. J., and Coauthors, 2018: All-sky satellite data assimilation at operational weather forecasting centres. *Quarterly Journal of the Royal Meteorological Society*, **144 (713)**, 1191–1217.

Harten, A., P. D. Lax, and B. v. Leer, 1983: On upstream differencing and godunov-type schemes for hyperbolic conservation laws. *SIAM review*, **25 (1)**, 35–61.

Kent, T., 2016: An idealised fluid model of numerical weather prediction: dynamics and data assimilation. Ph.D. thesis, School of Mathematics, University of Leeds.

Kent, T., O. Bokhove, and S. Tobias, 2017: Dynamics of an idealized fluid model for investigating convective-scale data assimilation. *Tellus A: Dynamic Meteorology and Oceanography*, **69 (1)**, 1369 332.

Kent, T., L. Cantarello, S. Tobias, G. Inverarity, and O. Bokhove, 2020: Idealized forecast-assimilation experiments for convective-scale numerical weather prediction, available at https://eartharxiv.org/repository/view/1921/.

Migliorini, S., and B. Candy, 2019: All-sky satellite data assimilation of microwave temperature sounding channels at the met office. *Quarterly Journal of the Royal Meteorological Society*, **145 (719)**, 867–883.

Pan, F., and R. B. Smith, 1999: Gap winds and wakes: Sar observations and numerical simulations. *Journal of the Atmospheric Sciences*, **56 (7)**, 905–923.

Petrie, R. E., R. N. Bannister, and M. J. P. Cullen, 2017: The "ABC model": a non-hydrostatic toy model for use in convective-scale data assimilation investigations. *Geoscientific Model Development*, **10**, 4419–4441.

Rabier, F., 2005: Overview of global data assimilation developments in numerical weather-prediction centres. *Quarterly Journal of the Royal Meteorological Society*, **131 (613)**, 3215–3233.

Rhebergen, S., O. Bokhove, and J. J. van der Vegt, 2008: Discontinuous galerkin finite element methods for hyperbolic nonconservative partial differential equations. *Journal of Computational Physics*, **227 (3)**, 1887–1922.

Rudd, A. C., I. Roulstone, and J. Eyre, 2012: A simple column model to explore anticipated problems in variational assimilation of satellite observations. *Environmental modelling & software*, **27**, 23–39.

Shrira, V., 1981: Propagation of long nonlinear waves in a layer of rotating fluid. *Sov. Phys. - Izvestija*, **17 (1)**, 55–59.

Shrira, V., 1986: On the long strongly nonlinear waves in rotating ocean. *Sov. Phys. - Izvestija*, **22 (4)**, 285–305.

Simmons, A. J., and A. Hollingsworth, 2002: Some aspects of the improvement in skill of numerical weather prediction. *Quarterly Journal of the Royal Meteorological Society*, **128 (580)**, 647–677.

Smith, P. J., A. M. Fowler, and A. S. Lawless, 2015: Exploring strategies for coupled 4d-var data assimilation using an idealised atmosphere–ocean model. *Tellus A: Dynamic Meteorology and Oceanography*, **67 (1)**, 27 025.

Stewart, L. M., S. L. Dance, and N. K. Nichols, 2013: Data assimilation with correlated observation errors: experiments with a 1-d shallow water model. *Tellus A: Dynamic Meteorology and Oceanography*, **65 (1)**, 19 546.

Vetra-Carvalho, S., S. Migliorini, and N. Nichols, 2011: Ensemble data assimilation in the presence of cloud. *Computers & Fluids*, **46 (1)**, 493–497.

Würsch, M., and G. C. Craig, 2014: A simple dynamical model of cumulus convection for data assimilation research. *Meteorologische Zeitschrift*, **23 (5)**, 483–490.

Zaplotnik, Ž., N. Žagar, and N. Gustafsson, 2018: An intermediate-complexity model for four-dimensional variational data assimilation including moist processes. *Quarterly Journal of the Royal Meteorological Society*, **144 (715)**, 1772–1787.

Zienkiewicz, O., R. Taylor, and P. Nithiarasu, 2014: *The Finite Element Method for Fluid Dynamics*. seventh ed., Butterworth-Heinemann, Oxford.

	H_2 [km]	H_1 [km]	θ_1^{obs} [K]	θ_2^{obs} [K]	U_1^{obs} [m/s]	U_2^{obs} [m/s]	η_0
2-layer troposphere	1.92	4.2	311.0	291.8	5.7	12.4	0.48

Table 1: Scaling of a 2-layer isentropic approximation of the troposphere obtained from radiosonde data during a Low Level Jet event on 10^{th}-11^{th} December 1977 in Brownsville, Texas (US). Variables labeled '1' refer to the upper layer, whereas those labeled with '2' refer to the bottom layer. We show in section §3 of part II how these values are computed and to what extent they justify the scaling chosen to derive the *ismodRSW* model.

Initial conditions	Fig. 5	η_0	0.48
Boundary conditions	Periodic	Z_0 [m]	$6.12 \cdot 10^3$
Relaxation solution	Fig. 5	c_0^2	1.8
τ_{rel}	4	α	6.0
CFL	0.1	β	2.0
θ_1 [K]	311	σ_c	0.21
θ_2 [K]	291.8	σ_r	0.24
Ro	0.248	L [km]	500
U [m/s]	12.4	N_{el}	400
T (L/U) [h]	11.2	Fr	0.36

Table 2: Model parameters associate to the *ismodRSW* nature simulation shown in Fig. 6. CFL indicates the Courant-Friedrichs-Lewy number. Please note that σ_c, σ_r and τ_{rel} are reported as non-dimensional variables. The Froude number Fr is computed as $\text{Fr} = U/\sqrt{g' H_2}$, with g' given by eq. (3) and H_2 from Table 1.

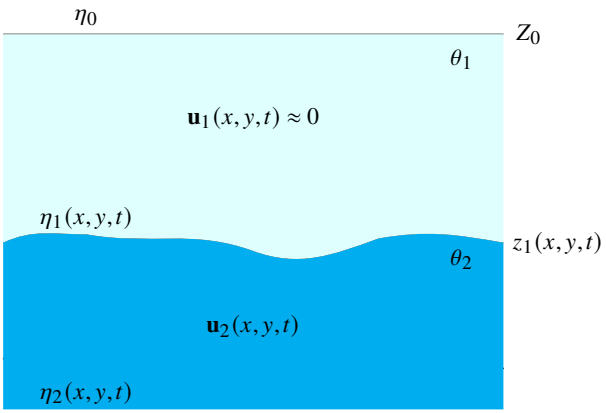

Figure 1: Schematic representation of the $1\frac{1}{2}$-layer isentropic shallow water model without topography ($b = 0$). Both the non-dimensional pressure η_0 and the fluid depth Z_0 are constant.

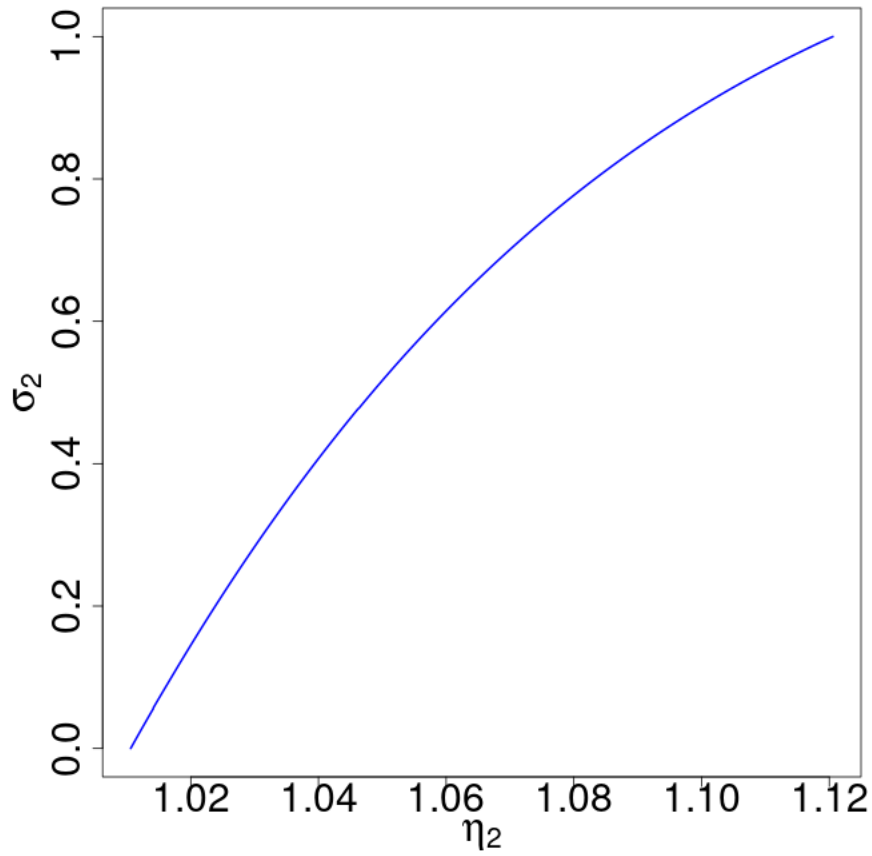

Figure 2: Plot of non-dimensional σ_2 as a function of η_2 for parameters: $R = 287\,\mathrm{J\,kg^{-1}\,K^{-1}}$, $c_p = 1004\,\mathrm{J\,kg^{-1}\,K^{-1}}$, $\theta_1 = 311\,\mathrm{K}$, $\theta_2 = 291.8\,\mathrm{K}$, $\eta_0 = 0.48$, $Z_0 = 6120\,\mathrm{m}$ and $g = 9.81\,\mathrm{m/s^2}$.

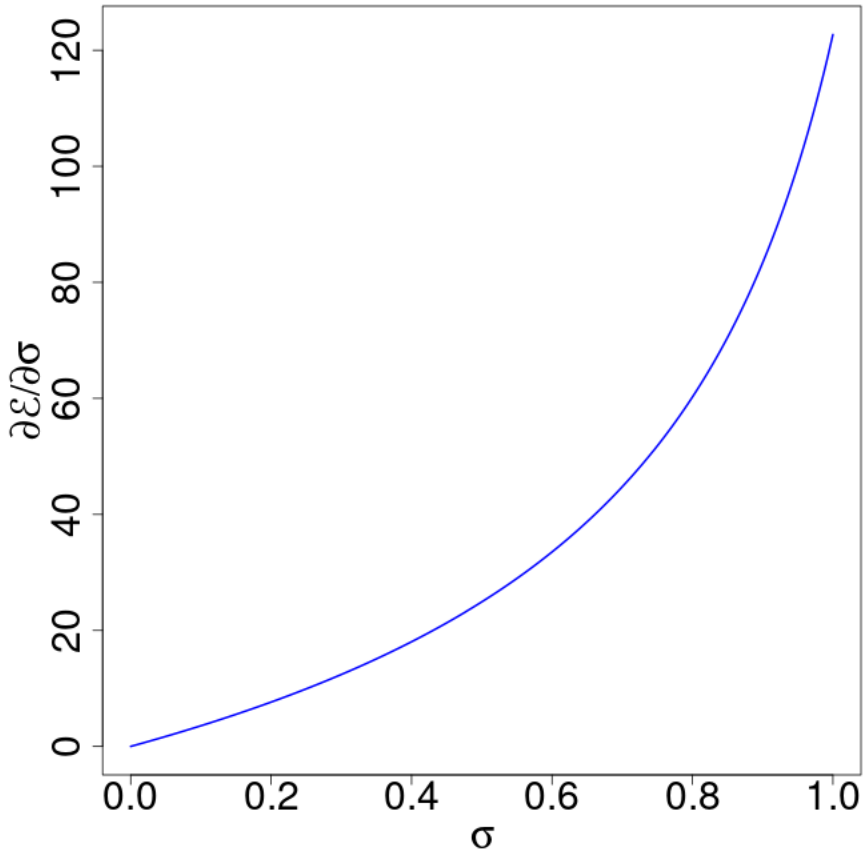

Figure 3: Plot of non-dimensional $\partial_\sigma \mathcal{E}$ as a function of σ for $R = 287\,\mathrm{J\,kg^{-1}\,K^{-1}}$, $c_p = 1004\,\mathrm{J\,kg^{-1}\,K^{-1}}$, $\theta_1 = 311\,\mathrm{K}$, $\theta_2 = 291.8\,\mathrm{K}$, $\eta_0 = 0.48$, $Z_0 = 6120\,\mathrm{m}$ and $g = 9.81\,\mathrm{m/s^2}$.

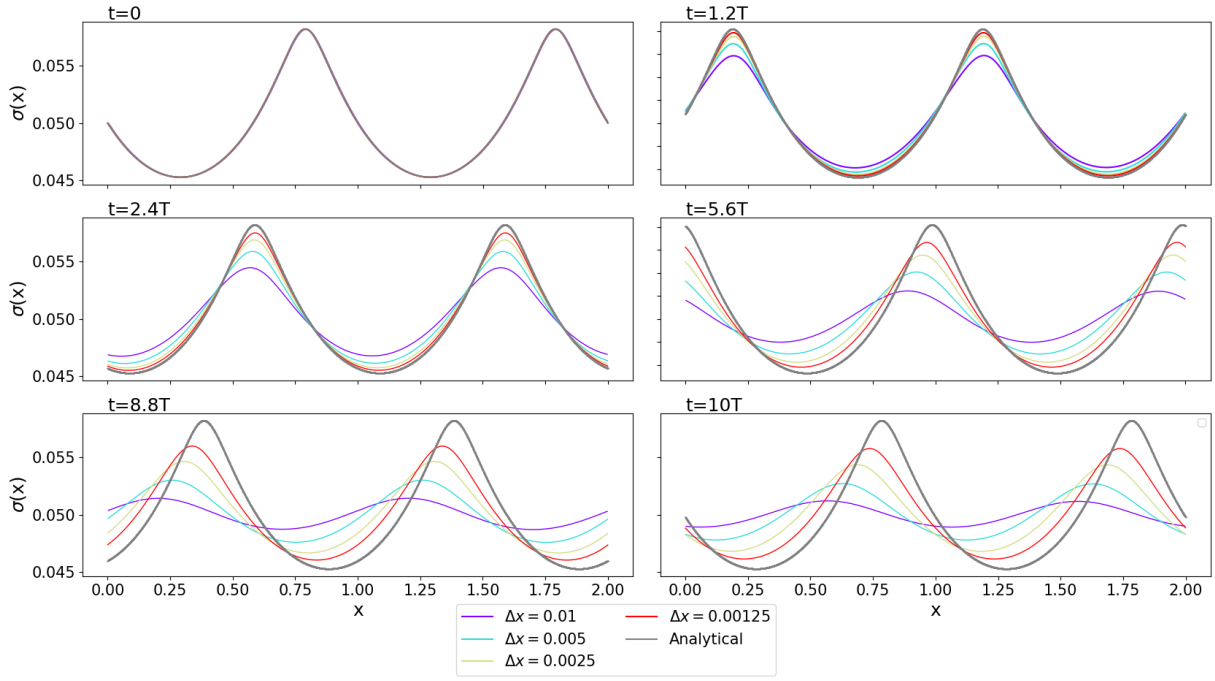

Figure 4: Comparison between Shira's analytical solution for σ translated in time (gray solid line) and the evolution of the model in (11) at various spatial resolutions initialised with the same solution. Snapshots after $\{0, 1.2, 2.4, 5.6, 8.8, 10\}$ periods (T) are shown. Initial conditions: $v_0 \equiv v(x,0) = 0.08$, $\chi_0 = 0$. Other parameters are: $\sigma_0 = 0.05$, $c = 23.05$, Ro $= 0.2305$, $c_p = 1004\,\mathrm{J\,kg^{-1}\,K^{-1}}$, $\theta_1 = 311\,\mathrm{K}$, $\theta_2 = 291.8\,\mathrm{K}$, $\eta_0 = 0.48$, $p_r = 1000\,\mathrm{hPa}$, $Z_0 = 6120\,\mathrm{m}$, CFL $= 0.5$.

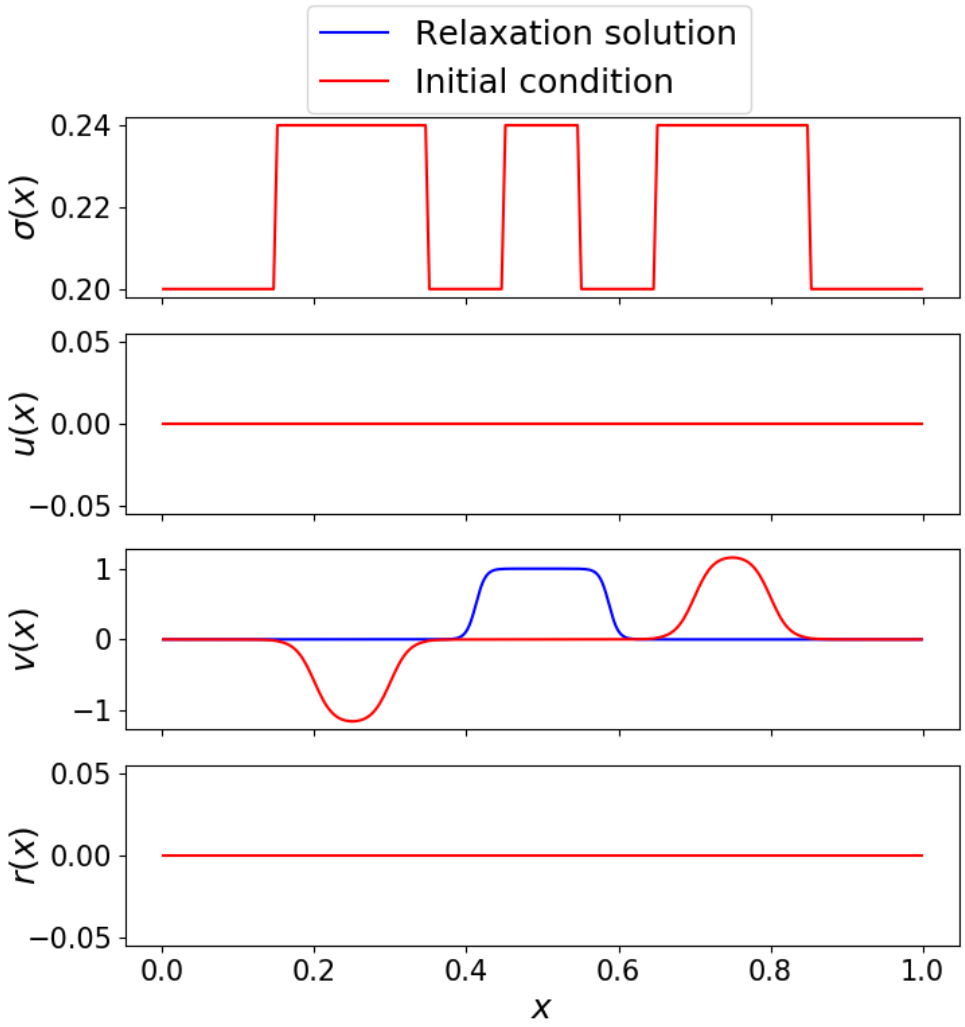

Figure 5: Initial condition (in red) and relaxation solution (in blue) of the nature run simulation (parameters listed in Table 2). All variables are non-dimensional.

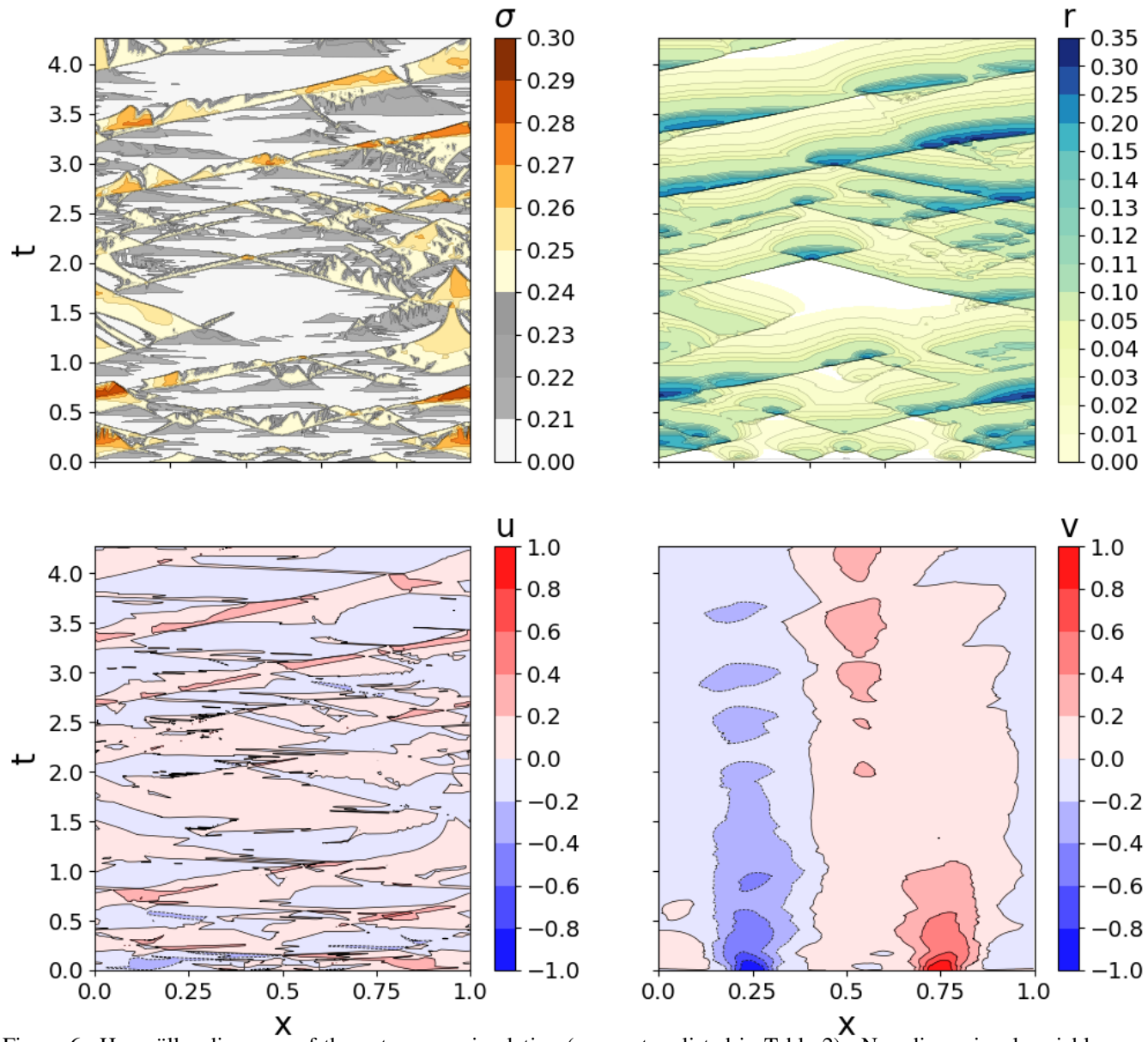

Figure 6: Hovmöller diagrams of the nature run simulation (parameters listed in Table 2). Non-dimensional variables: σ (top-left panel), r (top-right panel), u (bottom-left panel) and v (bottom-right panel). The gray and yellow shading in the top left panel indicates the areas where σ is above the convection (e.g. $\sigma_c < \sigma < \sigma_r$) and the rain threshold ($\sigma > \sigma_r$), respectively. Note that the length of the y axis ($t = [0, 4.272]$) is the non-dimensional equivalent of a 48 hours period, given the scaling in Table 2.

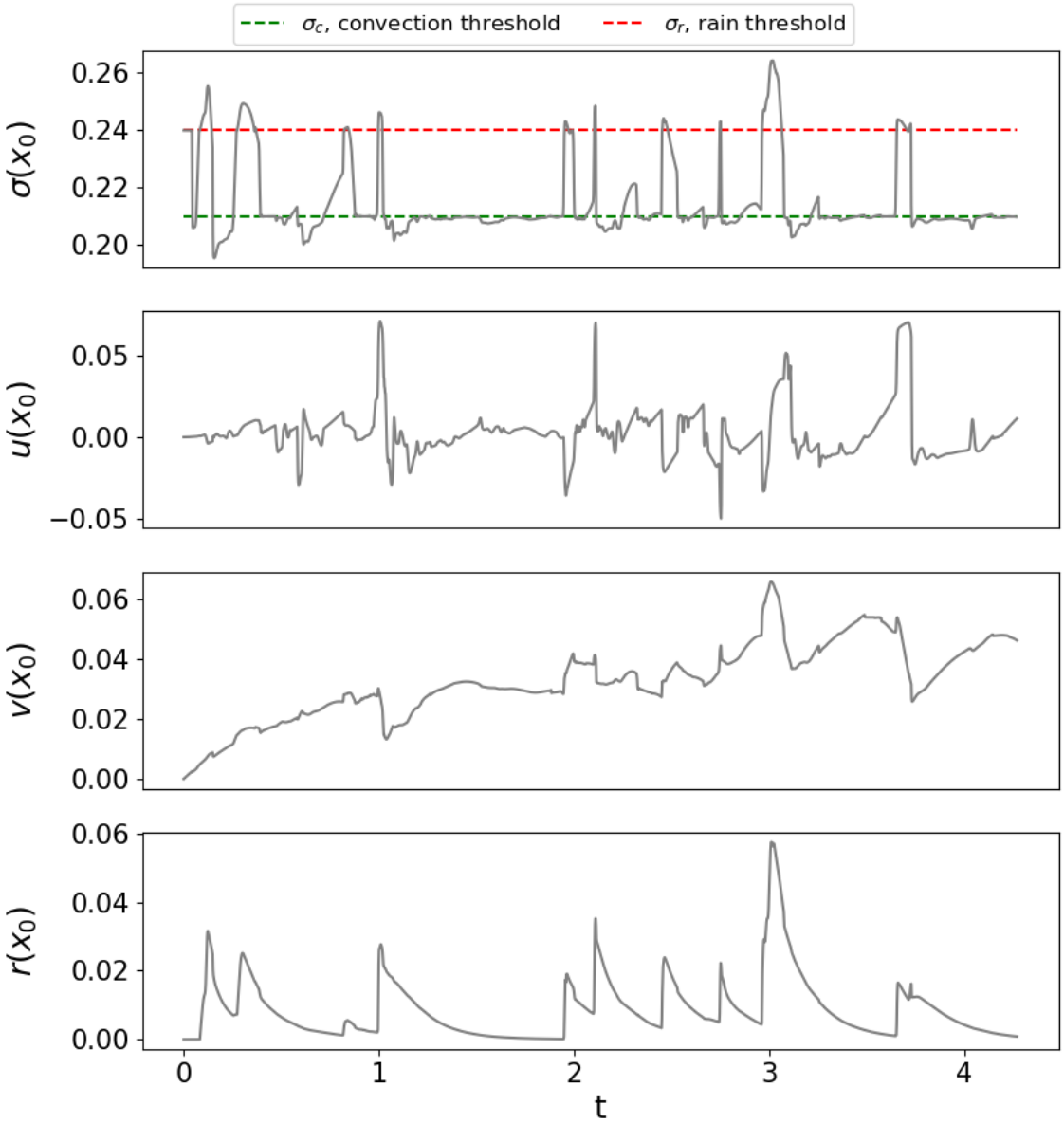

Figure 7: Time series of the nature run variable at location $x_0 = 0.5$ (parameters listed in Table 2).

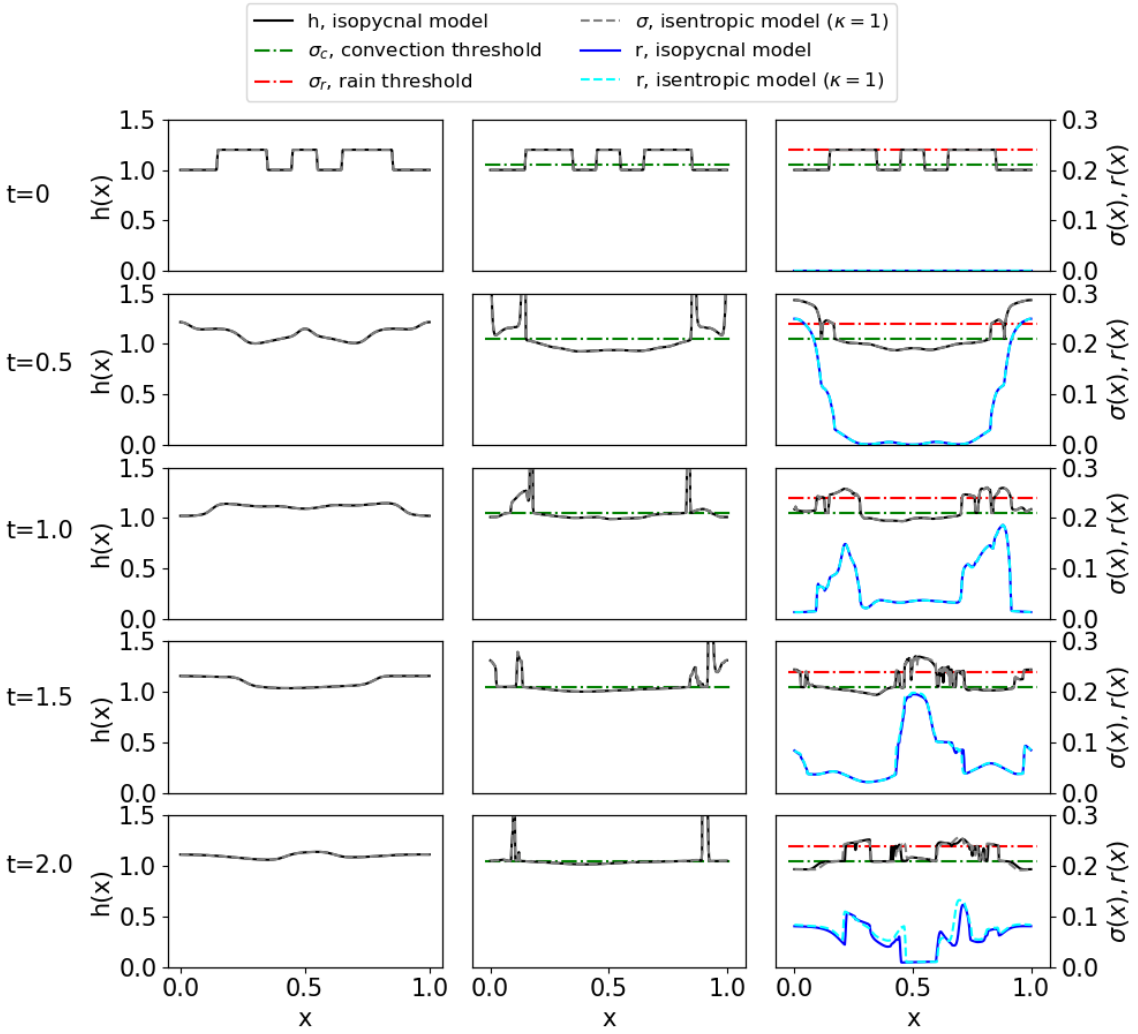

Figure 8: Comparison between the isopycnal and the isentropic model with $\kappa = 1$ at times (from top to bottom panels) $t = \{0, 0.5, 1.0, 1.5, 2.0\}$. Left panels: classic rotating shallow water with $\sigma_c, \sigma_r, H_c, H_r \to \infty$; central panels: convection-only regime with $\sigma_c = 0.21$, $H_c = 1.05$ (green dashed-dotted line) and $\sigma_r, H_r \to \infty$; right panels: fully modified shallow water with $\sigma_c = 0.21$, $H_c = 1.05$ and $\sigma_r = 0.24$, $H_r = 1.2$ (dashed-dotted red line). Variables: isopycnal fluid depth h (black solid line) and mass rain fraction r (blue solid line), isentropic pseudo-density σ (dashed gray line) and mass rain fraction r (cyan dashed line).